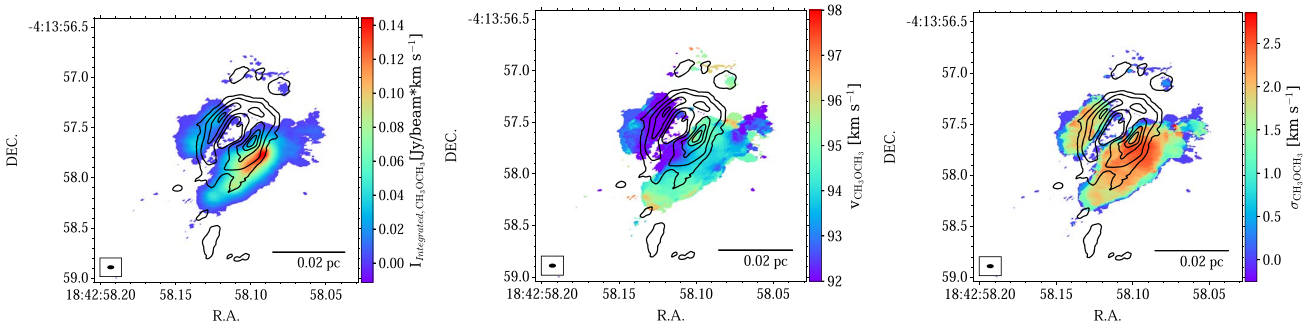

Figure 9. Moment 0, 1, and 2 maps (left to right) of $CH_3OCH_3(22_{4,19} - 22_{3,20}$, $E_{up} = 253.41$ K) emission, only including pixels that are above 1σ spectral rms (see Table 2, spw7). The black contours show the 1.3 mm continuum emission (0.5, 1, 1.5, 2, 2.5, 3, 3.5, 4, 4.5, 5, 5.5, 6 Jy arcsec^{-2}).

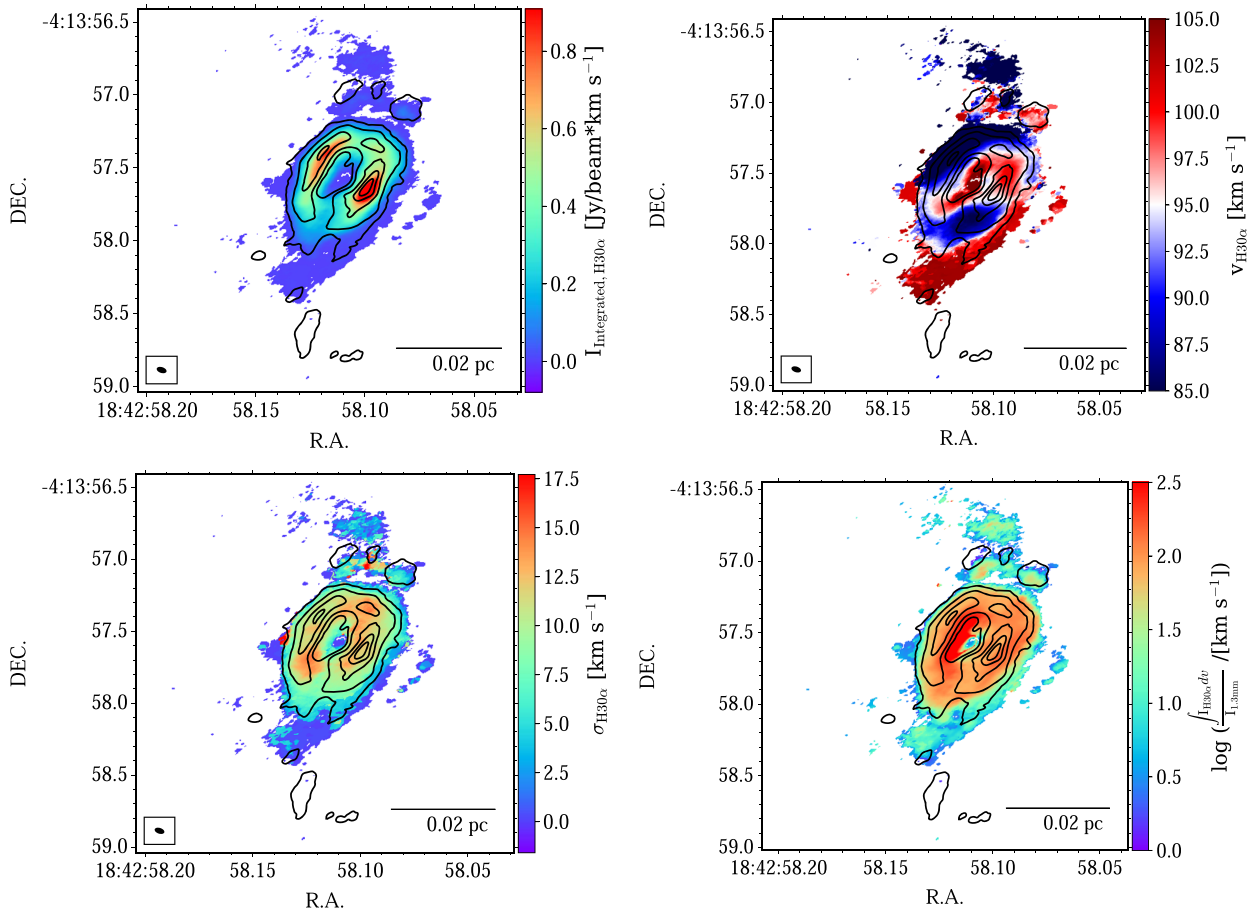

Figure 10. (a) Top left: H30α moment zero map, only considering pixels with integrated intensity above 5σ of the spectral rms measured over emission free velocity channels in the averaged velocity spectrum (note, $1\sigma \simeq 0.8$ mJy beam^{-1}). The black contours show the 1.3 mm continuum emission (0.5, 1, 1.5, 2, 2.5, 3, 3.5, 4, 4.5, 5, 5.5, 6 Jy arcsec^{-2}). (b) Top right: as (a), but now showing the H30α moment one map, i.e., averaged line-of-sight velocity. (c) Bottom left: as (a), but now showing the H30α moment two map, i.e., the 1D velocity dispersion along the line of sight of the H30α emission. (d) Bottom right: as (a), but now showing the ratio between the integrated intensity of H30α and the continuum intensity.

gradient to blueshifted velocities in the SE and redshifted velocities in the NW, with velocities differences of up to ± 10 km s^{-1} being observed. We will see later in Section 3.5 that this direction of the H30α velocity gradient is perpendicular to a large-scale CO outflow from the region. This fact suggests that rotation, either in a disk or in a disk wind, plays a role in setting this kinematic structure, which we discuss in more detail below. Other features seen in the moment 1 map include that the NE side of the ring and northern spur have blueshifted velocities, again by about 10 km s^{-1} from the systemic. The southern spur, which connects to the main millimeter continuum peak, shows redshifted velocities by up to about 10 km s^{-1} from the systemic. The moment 2 map shows that 1D velocity dispersions can exceed 10 km s^{-1} in the ring, but have much lower values in the northern and southern spurs.

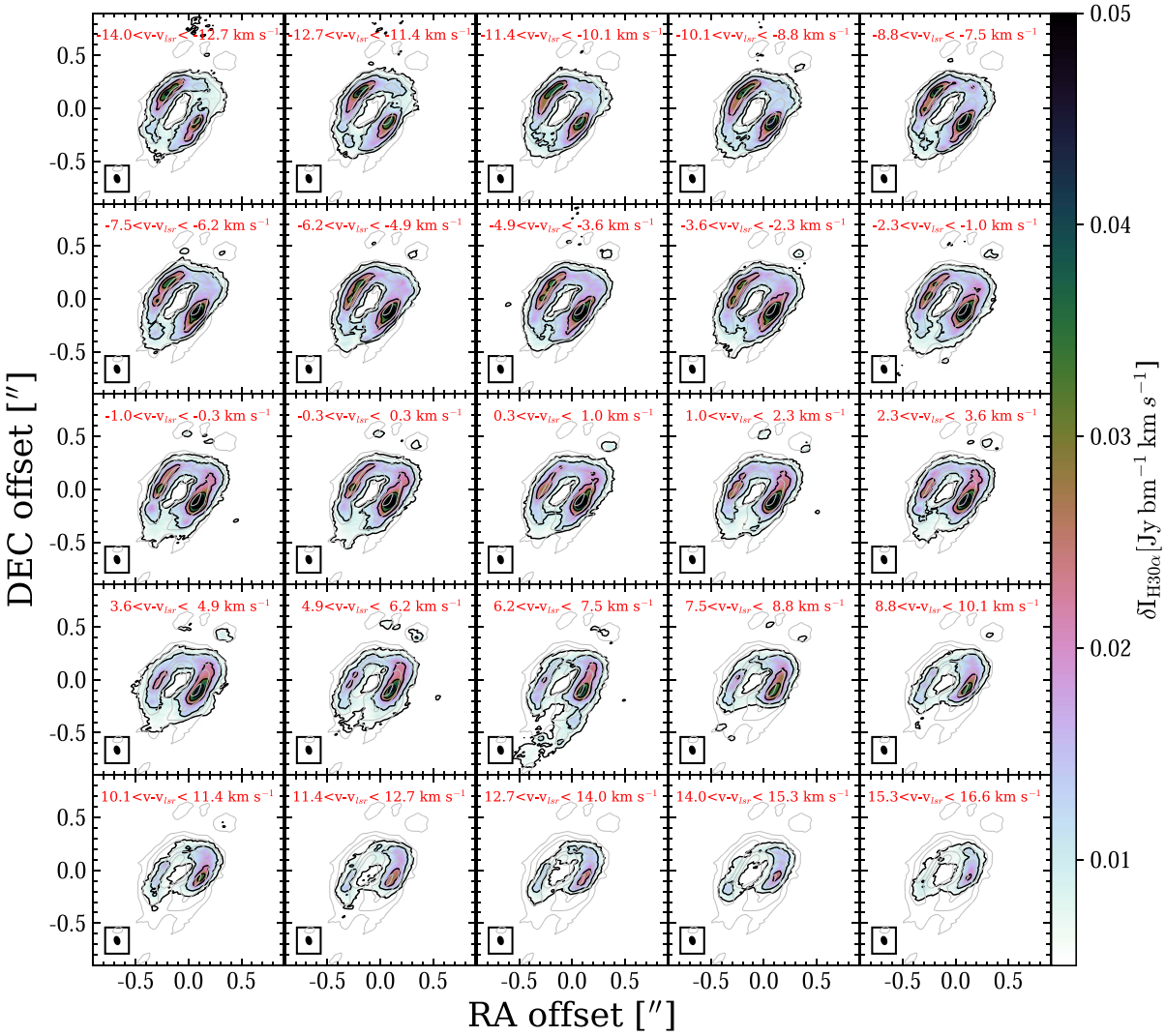

Figure 11. Channel maps of H30α emission based on C+I+E configurations. Each panel shows a moment 0 map integrated over the labeled velocity range. The synthesized beam is shown at the lower left corner of each panel. The overlaid C+I+E continuum contours (gray contours) have intensities 0.5, 1, 1.5, 2, 2.5, 3, 3.5, 4, 4.5, 5, 5.5, 6 Jy arcsec^{-2}.

The Figure 10 bottom right panel presents a map of the ratio of H30α integrated intensity to 1.3 mm continuum. The ratio between H30α integrated intensity and free–free continuum intensity for optically thin local thermodynamic equilibrium (LTE) conditions is (see, e.g., Zhang et al. 2019c)

$$\frac{\int I_{\rm H30\alpha} dv}{I_{\rm 1.3mm}} = \frac{4.678 \times 10^6 \text{ km s}^{-1} (T_{\rm e}/{\rm K})^{-1}}{[1.5 \ln(T_{\rm e}/{\rm K}) - 8.443](1 + N_{\rm He^+}/N_{\rm H^+})}. \quad (4)$$

For a fiducial ionized gas temperature of $T_{\rm e} = 10^4$ K and $N_{\rm He^+}/N_{\rm H^+} = 0.1$, we obtain a reference value for the ratio of 79 km s^{-1}. If the temperature is as low as 5000 K, then the value increases to about 200 km s^{-1}.

Most of the H30α emitting region shows line-to-continuum ratios $\lesssim$200 km s^{-1}, which could thus be consistent with optically thin LTE conditions. Some relatively low values could be due to the presence of dust contributions to the millimeter continuum, e.g., in the regions just outside the ring.

We next consider the implications of the kinematics of the H30α emission for the dynamics of the system. The spectrum of this emission extracted from a region with radius of 0″.3 around the main millimeter continuum peak is shown in Figure 12. If we attempt a virial analysis based on the velocity dispersion within this region, as was done above for CH_3OCH_3 emission, we find that the 1D velocity dispersion is 14.2 km s^{-1}, and so $M_{\rm dyn}$ given by Equation (3) is $\simeq$2000 $M_\odot$, i.e., >20 × larger than that inferred from CH_3OCH_3. We conclude that the H30α emission is most likely to be tracing an ionized wind that is escaping from the massive protostar. For example, this may be the ionized base of a rotating magneto-centrifugally launched disk wind. Such winds typically achieve speeds of the order of the escape speed from their launching radii, $r_{\rm dw}$, i.e.,

$$v_{\rm w,esc} = (2Gm_{*d}/r_{\rm dw})^{1/2} \rightarrow 23.0 \left(\frac{m_{*d}}{30\ M_\odot}\right)^{1/2} \left(\frac{r_{\rm dw}}{100 \text{ au}}\right)^{-1/2} \text{ km s}^{-1}, \quad (5)$$

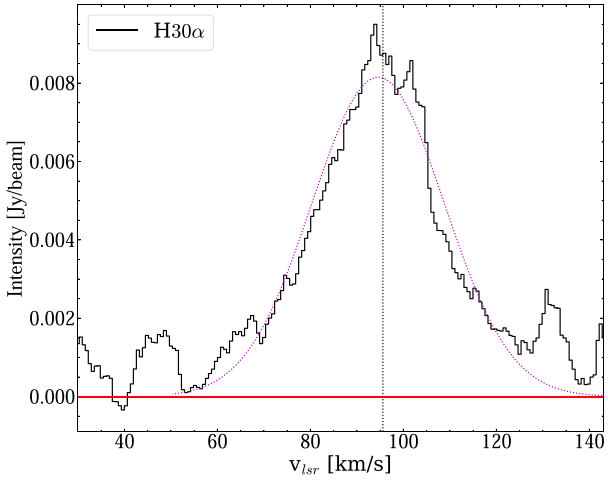

Figure 12. H30α averaged spectrum toward a circular aperture of 0″.3 radius from the main millimeter continuum peak. The red dotted line is the Gaussian fit to the spectrum. The corresponding dispersion is 14.2 km s^{-1}. The vertical black dotted line represents the systemic velocity of the source.

where m_{*d} is the mass of the star and disk enclosed within $r_{\rm dw}$. Inspection of Figure 12 reveals that there is high-velocity H30α-emitting gas out to at least 30 km s^{-1} to both redshifted and blueshifted velocities. The models of rotating ionized disk winds of (Tanaka et al. 2016, e.g., see their Figures 15 and 16) appear to be highly relevant to explain the general features of broad line width with the large-scale velocity gradient that we see in the H30α emission from G28.20-0.05.

3.5. Outflows Traced by CO, SiO, and NIR Emission

The ALMA spectral windows also include ^{12}CO(2–1), which we use to trace the presence of outflows. Figure 13 presents the moment 0 maps of ^{12}CO(2–1) emission: the blueshifted emission is integrated from +80 to +95 km s^{-1}; the redshifted emission is integrated from +96 to +115 km s^{-1}. Figure 14 presents channel maps of this ^{12}CO(2–1) emission. The overall morphology is that expected from a wide-angle bipolar outflow, with the P.A. of the near-facing blueshifted outflow axis being in the NE direction (i.e., PA $\sim$ 45°), consistent with being perpendicular to both the major axis of the main millimeter continuum peak and the direction of maximum velocity gradient of H30α emission. Note that there is some redshifted CO(2–1) emission in the NE direction (and some blueshifted emission in the SW direction), as would be expected in a wide-angle outflow. From the morphology shown in Figures 13(a) and (b), i.e., the projected lateral extent of the emission relative to the protostellar position, we estimate an opening angle (from outflow axis to outer extent of outflow projected on the sky) of the blueshifted outflow to be about 40°. This bipolar morphology is consistent with that reported in the study of Klaassen et al. (2011).

SiO line emission, also included in the ALMA spectral setup, is another tracer of outflows from massive protostars (e.g., Codella et al. 2013; Leurini et al. 2013). It is expected to be strong in regions of faster flows and/or strong shocks that may lead to destruction or sputtering of dust grains, which then enhances the gas phase abundance of SiO. Figure 13 shows blueshifted (+80 to +95 km s^{-1}) and redshifted (+96 to + 115 km s^{-1}) integrated intensity maps of SiO(5-4) emission. This emission is much sparser than the high-velocity CO(2–1) emission. The blueshifted SiO is again found mostly in the NE direction and at a narrower range of position angles from the protostar, i.e., apparently tracing the more central part of the cavity. Some redshifted emission is also seen in this region. The SiO emission is much weaker toward the SW side, where it is dominated by a modest knot of redshifted emission.

Figure 15 presents spectra of CO(2–1) and SiO(5-4) extracted from a region of radius 10″ centered on the protostar (based on C configuration data). In the CO spectrum, there is an absence of signal near the systemic velocity, likely due to absorption from ambient gas. CO emission is seen to extend to velocities that are up to about $\pm$25 km s^{-1} from the systemic velocity. On the other hand, the SiO(5-4) spectrum peaks near the systemic velocity, but also extends out to cover the same velocity range seen in CO(2–1).

Based on this extracted spectrum, Figure 16 presents an analysis of the CO-traced outflow mass and momentum, following the methods and assumptions of Zhang et al. (2019a) that were applied to similar data for the G339.88-1.26 massive protostar. The key assumptions of this method are the choice of CO abundance, i.e., $X_{\rm CO} = [^{12}{\rm CO}/{\rm H_2}] = 10^{-4}$, the choice of excitation temperature, i.e., $T_{\rm ex} = 10 - 50$ K (see also Dunham et al. 2014), and the assumption that the emission is optically thin. We follow Zhang et al. (2019a) to adopt a fiducial excitation temperature of 17.5 K, which minimizes the mass estimate from the (2–1) transition. A choice of $T_{\rm ex} = 50$ K would increase the mass by a factor of 1.5.

From this analysis, we obtain the following fiducial estimates that should be regarded as minimum values. We find masses of outflowing gas of 0.464 $M_\odot$ and 1.06 $M_\odot$ in the blueshift and redshifted components, respectively. These components have total momenta of 3.93 and 10.8 $M_\odot$km s^{-1}, respectively. The mean (mass-weighted) velocities of the components are thus 8.48 and 10.2 km s^{-1}, respectively. We associate the outflows with a size of 10″, i.e., $L_{\rm out} = 57{,}000$ au, and so the outflow timescales are 3.19×10^4 and 2.65×10^4 yr, respectively. Thus the mass flow rates are 1.46×10^{-5} and 4.00×10^{-5} $M_\odot$yr^{-1}, and the momentum injection rates are 1.23×10^{-4} $M_\odot$, and 4.07×10^{-4} $M_\odot$km s^{-1} yr^{-1}, respectively.

Figure 16 also shows the distribution of mass with velocity. Such distributions are important diagnostics that can be compared with theoretical models of massive protostellar outflows (e.g., Staff et al. 2019). In principle, such comparisons allow constraints to be placed on the evolutionary stage, the inclination of outflow axis to the line of sight, and other properties of the protostellar core.

The same figure also presents the mass spectrum of the outflow with a log-log scaling. In this panel, we also compare with the outflow mass spectra of G339.88-1.26 (Zhang et al. 2019a), which is more collimated and thus likely to be at an earlier evolutionary stage. We see that G28.20-0.05 has a more powerful low-velocity outflow than G339.88-1.26, but the latter has a larger amount of mass at high velocities. Some of these differences could be a result of varying degrees of inclination to the line of sight. However, we suspect that much of the fast outflowing gas that is closer to the outflow axis may have been photodissociated in G28.20-0.05, since this source is already starting to create a HC H II region. In this case, it is predicted that relatively broad and strong tracers of atomic outflow components are present, such as [O I] and [C II] lines.

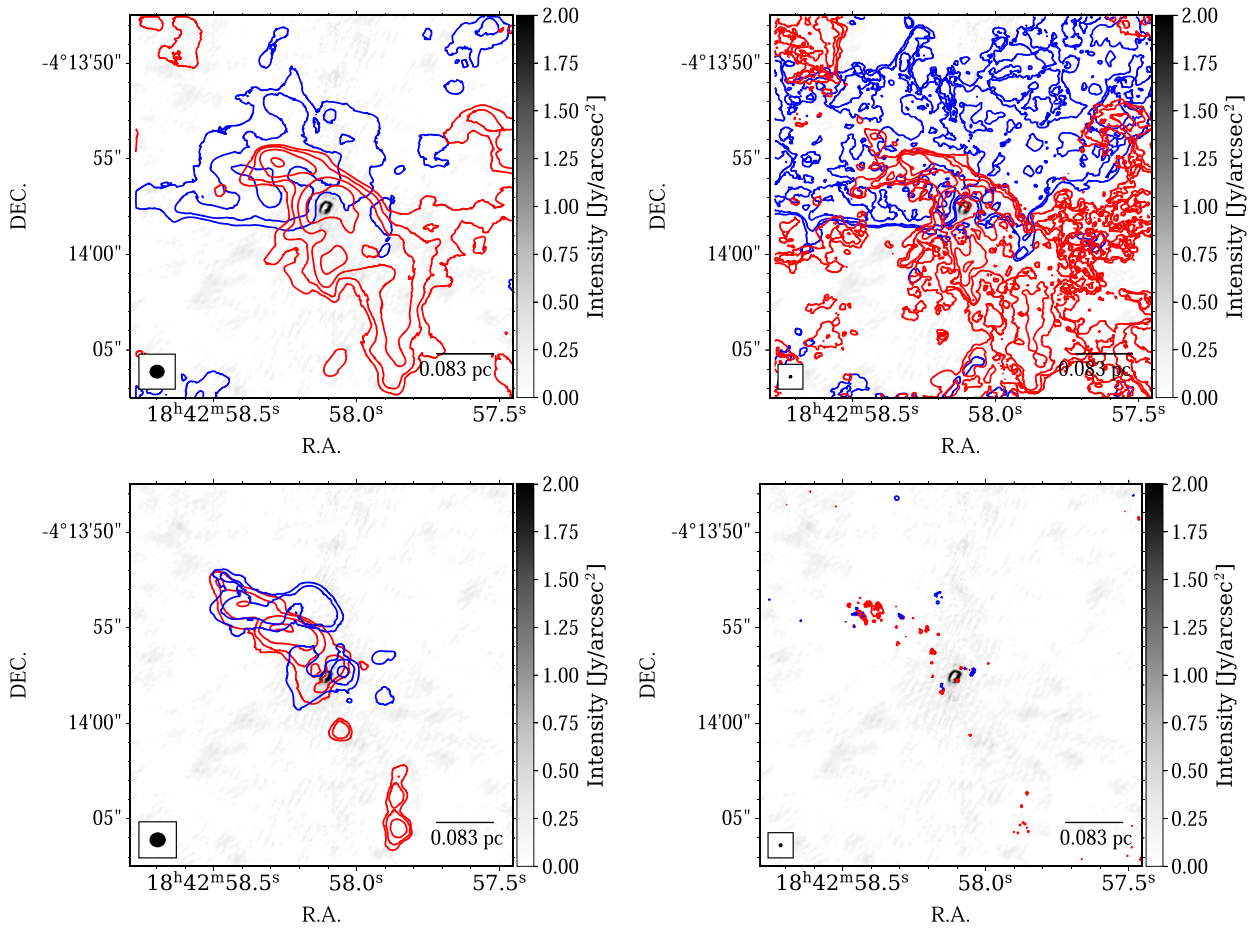

Figure 13. (a) Top left: integrated intensity maps of CO(2–1) emission tracing outflowing gas as observed in C configuration. The blue contours show blueshifted emission from +80 to +95 km s^{-1}. The contours levels are [1.28, 2.5, 5, 10, 20] Jy beam^{-1} km s^{-1}. The red contours show redshifted emission from +96 to +115 km s^{-1}. The contours levels are [1.28, 2.5, 5, 10, 20] Jy beam^{-1} km s^{-1}. Only pixels that are above 1σ spectral rms (=0.31 Jy beam^{-1}) are included. The gray scale shading shows the 1.3 mm continuum image (C+I+E). (b) Top right: as (a), but for C+I combined configurations of ^{12}CO(2–1) emission. The contours levels for the blueshifted and the redshifted emissions are [0.16, 0.32, 0.64, 1.28, 2.5, 5] Jy beam^{-1} km s^{-1}. (c) Bottom left: as (a), but now showing integrated intensity maps of SiO(5-4) emission (C configuration). The blue contours show blueshifted emission from +80 to +95 km s^{-1}. The red contours show redshifted emission from +96 to +115 km s^{-1}. The contours levels are [0.16, 0.32, 0.64, 1.28, 2.56, 5.12] Jy beam^{-1} km s^{-1}. Only pixels that are above 1σ spectral rms (=0.279 mJy beam^{-1}) are included. (d) Bottom right: as (c), but now for C+I combined configurations of SiO(5-4) emission. The contours levels are [0.01, 0.02, 0.04, 0.06, 0.08, 0.1, 0.12] Jy beam^{-1}.

To investigate if there is any further evidence of outflow activity, we observed the NIR emission in the region. Figure 17 shows the HST images in the *J* band (left panel) and in the *H* band (right panel) together with the ALMA band 6 continuum as cyan contours. The inner region near the millimeter continuum ring does not show significant emission at the shorter wavelengths, i.e., ∼1.1 μm. However, emission is clearly seen in the *H* band, i.e., at ∼1.6 μm, peaking at a position that is to the NE of the main millimeter continuum peak by about 0″.5 (i.e., ∼3000 au). This is the direction of the near-facing, mainly blueshifted outflow. Thus, one interpretation of the *H*-band emission is that it is scattered light from the massive protostar and/or inner accretion disk, which is able to reach us via a relatively low extinction path through the near-facing outflow cavity.

We use the HST images to measure–constrain the NIR fluxes from the source. This was done by performing circular aperture photometry using the Python package *photutils*[20] (Bradley et al. 2020) in both bands with an aperture size equivalent to ∼4 times the FWHM, which is about ∼0″.15, i.e., 6 pixels. We subtract the local background emission by measuring the median value of an annulus with inner and outer radii of 10 and 15 pixels, respectively. We centered the apertures at the peak of the emission in the *H* band and used the same location for the J (since no emission was found in this band). We applied a correction factor for the IR encircled flux[21] of 0.893 and 0.863 for the J and *H* bands, respectively, needed for the extracted aperture of ∼0″.6. We measure magnitudes in the HST Vega system of 23.48 and 18.98 for the J and *H* bands, respectively, although in the case of the *J*-band image only an upper limit was retrieved as we have a nondetection. Using the method described in Andersen et al. (2017), we transform the HST VEGAMAG system to Two Micron All Sky Survey (2MASS) system yielding magnitudes of 22.28 ± 0.14 and 18.04 ± 0.14, for the J and *H* bands, respectively. The

[20] https://photutils.readthedocs.io/en/stable/

[21] https://www.stsci.edu/hst/instrumentation/wfc3/data-analysis/photometric-calibration/ir-encircled-energy

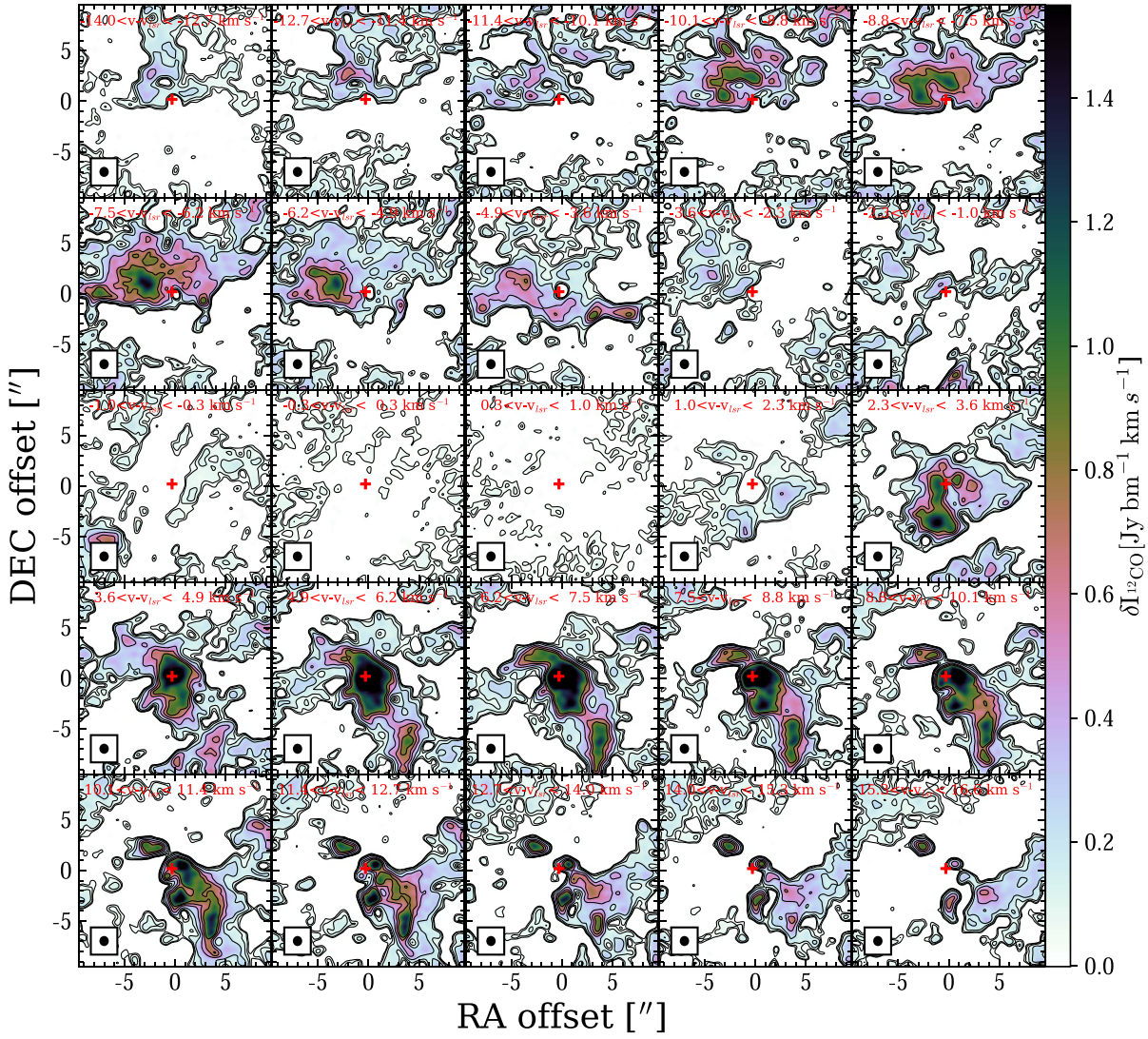

Figure 14. The C-only configuration channel maps of ^{12}CO(2–1) emission. Each panel shows the moment 0 map calculated within the labeled velocity range. The synthesized beam is shown in the lower left corner of each panel. The [0,0] point corresponds to the main continuum peak location (R.A.: 18:42:58.09979, decl.: −04:13:57.64121) and is marked by the red "+" symbol.

uncertainties in the magnitudes are dominated by the uncertainties in the transformation to 2MASS (see, e.g., Andersen et al. 2017).

A lower limit on the amount extinction to the source based on the J and H magnitudes was calculated using the extinction law of Rieke & Lebofsky (1985). This law relates the extinction in J (A_J) and in H (A_H) with the visual extinction (A_V) through $A_J = 0.282A_V$, $A_H = 0.175A_V$. If we assume an intrinsic color of −0.164 for an O9V type star taken from Table 5 of Pecaut & Mamajek (2013), this results in a lower limit in the visual extinction of $A_V > 41$ mag, corresponding to mass surface density $\Sigma = 1.83 \times 10^{-4}$ g cm^{-2} assuming a conversion factor from A_V(mag) to $N_{\rm H}^{\rm NIR}$ (cm^{-2}) of 1.9×10^{21} cm $^{-2}$ (A_V/mag) (Bohlin et al. 1978) and $\Sigma = 1.4 m_{\rm H} N_{\rm H}^{\rm NIR}$ g cm^{-2}.

The HST observations also included the F128N and F164N narrowband filters designed to detect Paβ (1.28 μm) emission from ionized gas and [Fe II] (1.64 μm), which is a tracer of outflow shocks (e.g., Fedriani et al. 2019). However, no significant emission was detected in these continuum-subtracted images toward the protostar nor in the larger scale outflow. One possible explanation for this is the relatively large amount of extinction of this region.

4. Protostellar Properties from SED Modeling

Light from the protostellar photosphere is expected to be mostly absorbed by dust in the surrounding disk and infall envelope and then be reprocessed into the infrared. The MIR to far-IR (FIR) SED can thus be used to constrain protostellar properties. The most direct observable is the bolometric flux ($F_{\rm bol,iso}$), i.e., integrating over the SED. Then, given the distance to the source and accounting for foreground extinction, one can estimate the isotropic bolometric luminosity ($L_{\rm bol,iso}$), i.e., assuming the protostar emits isotropically.

In the context of core accretion models for massive star formation, Zhang & Tan (2018) have presented a grid of model protostellar SEDs that depend on the initial mass of the core

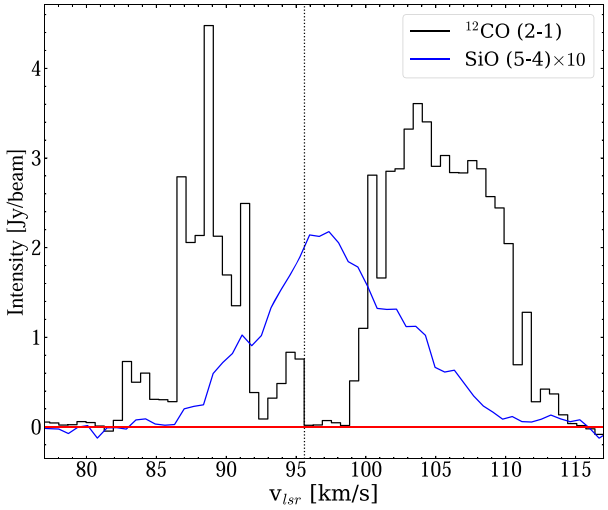

Figure 15. CO(2–1) and SiO(5-4) averaged spectra extracted from a circular aperture of radius 10″.

(M_c), the mass surface density of the clump environment ($\Sigma_{\rm cl}$), and the evolutionary stage as parameterized via the current protostellar mass (m_*). Two additional parameters that influence the SED are the viewing angle to the outflow axis ($\theta_{\rm view}$) and the level of foreground extinction (A_V). All other core properties, such as initial core radius (R_c), current accretion rate ($\dot{m}_*$), intrinsic bolometric luminosity ($L_{\rm bol}$), and outflow opening angle ($\theta_{\rm w,esc}$), are determined from M_c, $\Sigma_{\rm cl}$, and m_*. Here we determine the protostellar model parameters that best match the SED of G28.20-0.05.

To constrain the protostellar MIR to FIR SED we utilize data from Spitzer-IRAC, SOFIA-FORCAST/HAWC+, and Herschel-PACS/SPIRE (see Table 3). We note that the IRAC fluxes are used only as upper limit constraints, since the models do not include polycyclic aromatic hydrocarbon emission or emission from transiently heated small grains. We note also that millimeter to centimeter fluxes from ALMA, VLA, and ATCA are not used here to constrain the protostellar models. We follow methods of SED determination and fitting developed for the SOMA star formation survey (De Buizer et al. 2017; Liu et al. 2019, 2020; Fedriani et al. 2022). The latest version of these methods involve choosing the radius of a circular aperture ($R_{\rm ap}$) for the source objectively by examination of the Herschel 70 μm image (when available). The radius is set at the point at which a further increase of 30% in radius leads to the background-subtracted flux increasing by <10%. For background estimation, the method evaluates the average intensity of emission in an annulus from $R_{\rm ap}$ to $2R_{\rm ap}$ and assumes this applies over the area of the source aperture in order to derive the background-subtracted flux. The uncertainties in the fluxes are assumed to be a combination of 10% systematic uncertainty, e.g., due to flux calibration, and a contribution from the background, which here is set equal to the background flux. In the case of G28.20-0.05, the derived aperture radius has an angular size of 15″.5 (see Figure 1(b)), corresponding to 0.43 pc.

Figure 18 shows the SED of the protostar. We see that F_ν appears to peak around 70 μm. The uncertainties due to background subtraction are seen to become significant at longer wavelengths, which reflects the fact that the protostar is surrounded by large quantities of relatively cool, dusty gas. For completeness, Figure 18 also shows the fluxes from ALMA, VLA, and ATCA. These are seen to be enhanced with respect to the expected trend of thermal emission, indicating that they are dominated by or have significant contributions from ionized gas. We also note that these millimeter to centimeter fluxes are not evaluated with the same aperture as used at shorter wavelengths and, being measured by interferometers, are subject problems of missing flux.

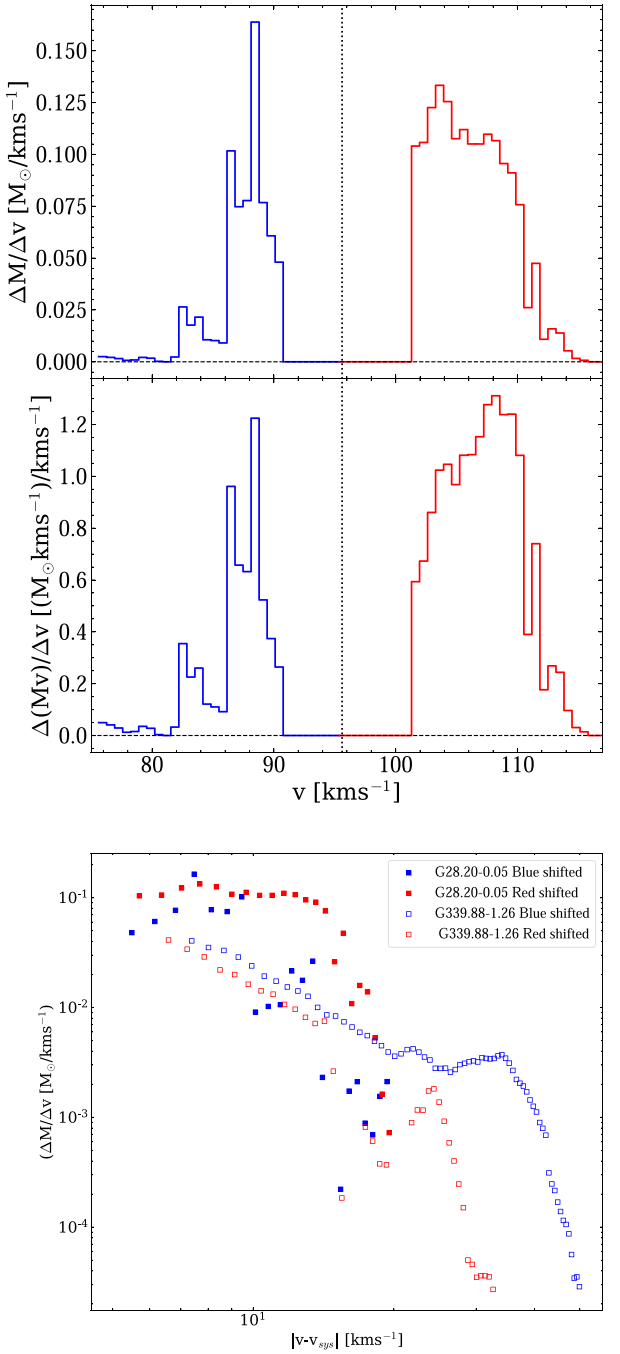

Figure 16. (a) Top: distribution of outflow mass inferred from CO(2–1) vs. velocity. (b) Middle: distribution of outflow momentum inferred from CO(2–1) vs. velocity. (c) Bottom: mass spectra of blueshifted and redshifted outflow components. The equivalent data from the G339.88–1.26 massive protostar (Zhang et al. 2019a) are also shown.